Scatter Correction for C-Arm CT Using Primary Modulation

Bastian Bier, Kerstin Müller, Martin Berger, Jang-Hwan Choi, Ludwig Ritschl, Marc Kachelrieß, Rebecca Fahrig and Andreas Maier

***Abstract*—Cone-beam computed tomography (CBCT) suffers from a large amount of scatter, resulting in severe scatter artifacts in the reconstructions. Recently, a novel scatter correction approach was introduced using a primary modulator, which is inserted between the X-ray source and the object. The method showed promising results, but was tested on a table-top X-ray system only. In our work, this method is transferred to a clinical C-arm CBCT. Extensions are added to compensate for scanner motion and tube current modulation. We show that scatter correction using primary modulation is possible on a clinical CBCT: scatter artifacts in the reconstructions were able to be removed with the newly extended method. Compared to a slit scan, our approach showed superior results with an improvement of the contrast-to-noise ratio.**

***Index Terms*—C-Arm CBCT, Primary Modulator, Reconstruction, Scatter Correction.**

I. Introduction

SCATTERED radiation is a major problem in CBCT, resulting from the large irradiated volume and the large area covered by the detector of such systems. The amount of scatter measured on the detector often exceeds the measured primary radiation, causing a high scatter-to-primary ratio (SPR) [1]. This has a severe impact on the reconstructions' image quality, where the scatter induces cupping and shadow artifacts as well as contrast loss [2].

Therefore, scatter correction methods are essential in order to remove these artifacts. Existing methods can be divided into hardware-based scatter rejection methods and software-based scatter correction methods [2]. Approaches among the first category are the antiscatter grid (ASG) [3], air gaps [4] and collimation. They are similar in that the geometry and the hardware of the X-ray system are manipulated to reduce measured scatter. Software-based techniques are either based on measurements [5], statistics or deterministic [6]. Hardware and software-based approaches are often combined in order to achieve a clinically satisfying image quality.

Another scatter correction method uses a primary modulator, which is inserted in between the X-ray source and the object. The modulator consists of semitransparent blocks alternating with transparent ones. This pattern modulates the primary radiation and leaves the scattered radiation untouched, which facilitates scatter estimation either in the frequency domain [7], [8] or the in the spatial domain [9]. The latter method was published recently and is called *improved Primary Modulator Scatter Correction (iPMSE)*. The iPMSE method showed promising results, but was tested on table-top X-ray systems only, where the imaging geometry and the X-ray spectrum is constant for all projections.

B. Bier, M. Berger and A. Maier are with the Department of Computer Science, Pattern Recognition Lab, Friedrich-Alexander-University Erlangen-Nuremberg, Germany.

K. Müller, J. Choi, L. Ritschl and R. Fahrig are with the Department of Radiology, Stanford University, Stanford, CA, USA. L. Ritschl and R. Fahrig are now with Siemens Healthcare GmbH, Forchheim, Germany.

M. Kachelrieß is with the Medical Physics in Radiology, German Cancer Research Center (DKFZ), Heidelberg, Germany.

Corresponding author: bastian.bier@fau.de

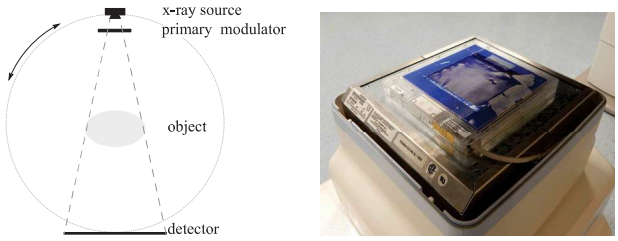

(a) Imaging geometry of the C-arm system with a primary modulator.

(b) Primary modulator mounted on top of the X-ray source.

Fig. 1: Imaging geometry with a primary modulator.

In this work, the iPMSE algorithm is extended and transferred to a clinical C-arm CBCT. The imaging geometry of our experimental setup is shown in Figure 1a. The X-ray source and the detector rotate around the object with the modulator mounted on top of the source, as can be seen in Figure 1b. The wobble of the C-arm during rotation as well as the tube current modulation of the system affect the projected modulator pattern. A solution to these problems is proposed by approximating the amplitude and the position of the modulator pattern. In the following, we call this extended algorithm *C-arm iPMSE*.

II. Materials and Methods

A. Theory

1) The iPMSE algorithm: The iPMSE algorithm requires two projection images, as can be seen in Figure 2. The first image is a projection of the primary modulator only, hereafter referred to as reference modulator pattern $\boldsymbol{M}$. The second image is a projection of the object and the primary modulator $\boldsymbol{c}_m$. The algorithm estimates the scatter image $\boldsymbol{c}_s$ with a gradient-based optimization function [9]. From that, the scatter-corrected projection $\boldsymbol{c}_p$ is obtained:

$$\boldsymbol{c}_p = \boldsymbol{M}^{-1} \cdot (\boldsymbol{c}_m - \boldsymbol{c}_s). \tag{1}$$

In $\boldsymbol{M}^{-1}$, each element is the inverse of the value in $\boldsymbol{M}$. Equation 1 shows that $\boldsymbol{M}^{-1}$ must have the same amplitude

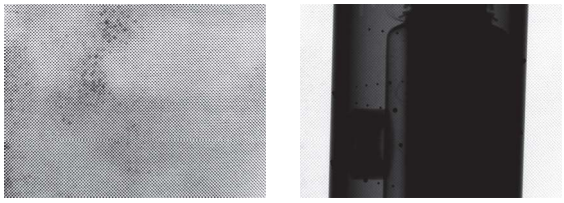

(a) Projection of the modulator $\boldsymbol{M}$.

(b) Projection of the modulator and the object $\boldsymbol{c}_m$.

Fig. 2: Projections required for the iPMSE algorithm.

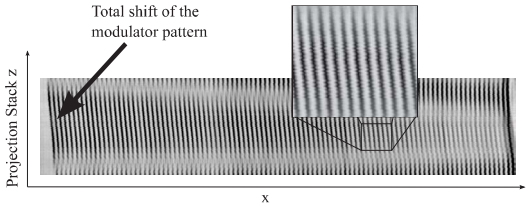

Fig. 3: The reordered projection stack of a modulator acquisition shows two motion effects: a total shift and small deviation in the pattern in adjacent projections.

and position as the modulator pattern in projection $\boldsymbol{c}_m$, otherwise residual modulator patterns persist in the corrected projection image and the scatter estimate may be incorrect.

2) Motion of the Projected Modulator Pattern: In rotations over 200°, the C-arm wobbles and deforms, causing a different position of the projected modulator pattern for each angle. The low-frequent deformation between the X-ray source and the detector is due to the effect of the gravity on the rotating C-arm and results in a total shift of around 15 pixels in the projected modulator pattern. This is indicated by the arrow in the reordered modulator projection stack, shown in Figure 3. The high-frequent wobble of the C-arm causes a sub-pixel shift in the pattern in adjacent projections. This effect is visible in the zoomed-in part in Figure 3, where this motion results in jagged lines.

3) Amplitude Change in the Projected Modulator Pattern: Clinical C-arm systems have a tube current modulation system, which adjusts the exposure parameters (tube voltage, exposure time and tube current) during the acquisition [10]. The changing tube voltage results in a varying modulation amplitude due to the energy-dependent attenuation of the modulator material for different X-ray source intensities as well as in a changing amount of emitted photons, which has to be corrected for.

B. Scatter Correction Workflow: C-arm iPMSE

Figure 4 shows the workflow of the new C-arm iPMSE method. The open-source software framework CONRAD [11] is used for the processing and reconstruction of the projection images. The acquired raw images are preprocessed [12] to obtain the projections in the intensity domain, where the scatter estimation takes place.

1) Establishment of a Modulator Database: The database contains reference projections of the modulator pattern acquired at various tube voltages and angles. Each projection is averaged to reduce noise. This is accomplished by acquiring three, 3D, rotational modulator acquisitions for each tube voltage. For each of the 248 angles, the corresponding projections of the acquisition as well as their direct neighbors are averaged. We acquired projections at 70 kVp, 90 kVp, 110 kVp and 120 kVp for the database. The reference modulator pattern M is then created from these projections.

2) Approximation of the Modulator Amplitude with Linear Interpolation: For each projection c_m, a reference modulator pattern is created, which has the same amplitude as the modulator in the projection c_m itself. This is achieved through a linear interpolation of two modulator patterns in the database, which are acquired at the same angle as projection c_m and at voltages next to projection c_m. This results in an approximation for M with a similar amplitude as the modulator pattern in the projection c_m.

3) Block Matching Registration: The reference modulator pattern M is aligned to the pattern in the projection c_m in a block matching registration step. The algorithm divides the reference projection image into sub blocks of 15 pixels. For each block, a translation, which optimizes the correlation coefficient, is calculated. The sub-pixel accuracy is set to 0.1 pixels and the search radius to 1.5 pixels. All translations are sorted according to their correlation coefficient, and the median translation of the translations corresponding to the highest 10 % is computed. This translation is applied to the reference modulation pattern. The difficulty in the registration is that the modulator pattern is hardly visible in projection c_m. The block matching registration shows robust results, since it uses the information from the entire projection and applies the translation with the best correlation matches. The search radius is restricted to a small area, because the initial estimate for M is already close the correct position, having been created from projections acquired at the same angle.

4) iPMSE: After the amplitude approximation and the registration step, the standard iPMSE algorithm as described in [9] is applied. A part of an iPMSE-corrected projection without and with the proposed extensions is shown in Figure 5a and Figure 5b, respectively. A residual modulator pattern is clearly visible in Figure 5a and is even more apparent in the difference image shown in Figure 5c. This pattern disappears with the new extended method.

C. Postprocessing

The negative logarithm is applied to the scatter-corrected images to obtain projections in the line-integral domain, followed by a noise suppression as suggested by Zhu et al. in [1]. This is essential since noise increases in scatter-corrected projection images [7], [1]. Without a suitable noise suppression, the benefits of the scatter correction can be lost due to the high increase of the noise level. Subsequently, a truncation correction, the standard FDK reconstruction algorithm with the Shepp-Logan kernel, and a ring artifact correction are applied [6].

III. Experiments and Results

All acquisitions were conducted with the Siemens zeego C-arm system (Siemens Healthcare GmbH, Forchheim, Germany). The focal spot size was set to 0.3 mm to reduce the

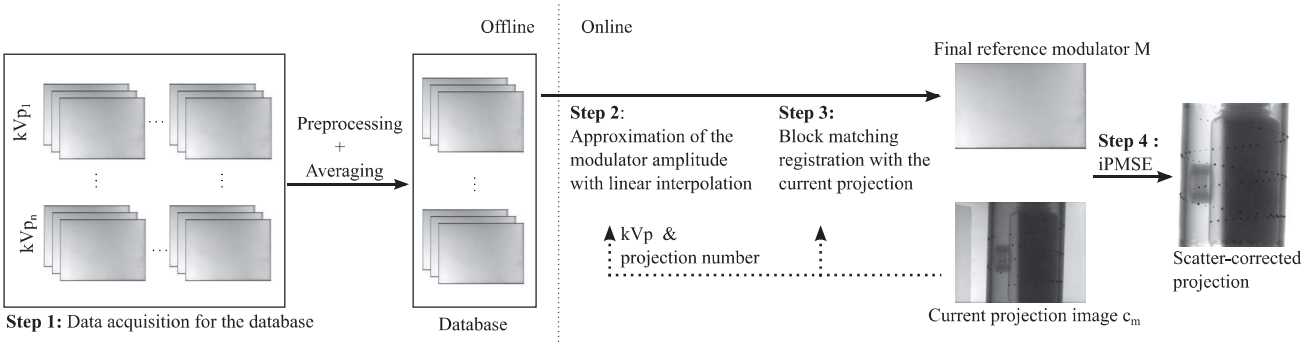

Fig. 4: Workflow of the proposed C-arm iPMSE method. Step1: Establishment of a modulator database. Step 2: Approximation of the modulator amplitude. Step 3: Block matching registration. Step 4: iPMSE algorithm.

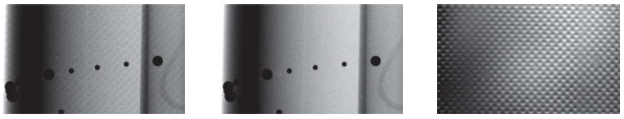

(a) iPMSE-corrected. (b) C-arm iPMSE-corrected. (c) Difference image.

Fig. 5: Parts of iPMSE-corrected projections without and with the added extensions. Residual modulator pattern is removed with the C-arm iPMSE algorithm.

(a) Phantom for Experiment 1. (b) Phantom for Experiment 2.

Fig. 6: Electron density phantom used for the experiments.

penumbra effect. 248 projections with a size of 1240×960 pixels were acquired during one rotation covering 200°. The material of the modulator was erbium, its thickness 0.0252 mm and the block size 0.457 mm (as in [9]). The transmission of the semitransparent blocks at 120 kVp was approximately 80% [13].

Two experiments with different objectives were performed. In both, the Electron Density Phantom (EDP) was scanned (CIRS, Norfolk, VA, USA). The phantom for Experiment 1 is shown in Figure 6a. Two torso shaped objects were placed next to the EDP in order to cause a large amount of scatter and attenuation. The phantom for Experiment 2 is shown in Figure 6a. Only the inner part of the EDP was scanned with an additional water bottle and the plugs from the EDP were placed next to the phantom. Due to its elliptical shape, the tube voltage varied in between 90 and 120 kVp in contrast to the constant tube voltage of 125 kVp in Experiment 1. Further, Experiment 1 was conducted with and without an ASG whereas Experiment 2 was only with ASG.

Figure 7 shows the center slices of the corrected and non-corrected reconstructions of the aforementioned experiments. The first two rows show the results of Experiment 1 with

TABLE I: Average CNR of the ROIs shown in Figure 8.

	Exp. 1 no ASG	Exp. 1 with ASG	Exp. 2
No Correction	2.39	2.61	2.32
Slit Scan	3.24	2.92	6.51
C-arm iPMSE	**5.98**	**6.01**	**8.62**

and without the ASG. The last row shows the results of Experiment 2. The first reconstruction in each row is without a scatter correction. All scatter artifacts are present: shadow and cupping artifacts as well as contrast loss. The second column shows reconstructions of a slit scan where the z-collimator aperture, i.e. the field of view (FOV) in z-direction, was minimal in order to reduce the irradiated volume. This has been shown to reduce the amount of scatter and thus should yield better results. Regardless, the scatter artifacts persisted in these reconstructions, although the cupping artifact was slightly suppressed. The last column shows reconstructions using the newly C-arm iPMSE method. Scatter artifacts were successfully removed. A small cupping artifact was visible at the border region of the FOV, which may have also resulted from object truncation. In Figure 8c, line profiles of reconstructions from Experiment 1 and 2 are shown. In the line profiles of the non-corrected and the slit scan reconstruction, the cupping artifact is given by increasing values towards the boundary of the FOV. This artifact disappeared, however, upon using the new method. Further, we computed the contrast-to-noise ratio (CNR) in the reconstructions for nine region-of-interests (ROI) shown in Figure 8a and Figure 8b. Table I shows that the averaged CNR improves in the scatter-corrected reconstructions towards the scatter-distorted and the slit scan reconstructions. In regions with dense material, slight streak artifacts were introduced in the scatter-corrected reconstructions.

IV. Discussion

Incorporating the iPMSE method into a clinical C-arm CT showed promising results. Our new method was able to remove most of the scatter artifacts and could substantially improve the image quality compared to a slit scan. In particular, the disappearance of the cupping and the shadow artifact improved the image quality clearly. Currently, streaking artifacts appear in

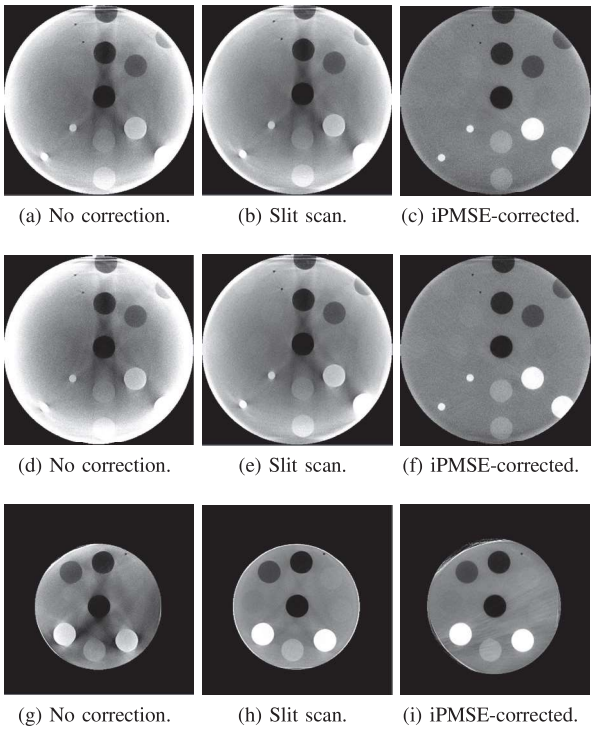

(a) No correction. (b) Slit scan. (c) iPMSE-corrected.

(d) No correction. (e) Slit scan. (f) iPMSE-corrected.

(g) No correction. (h) Slit scan. (i) iPMSE-corrected.

Fig. 7: Reconstruction images. First row: Experiment 1 with ASG. Second Row: Experiment 1 without ASG. Third row: Experiment 2 with ASG. Window level [-1000HU, 1000 HU].

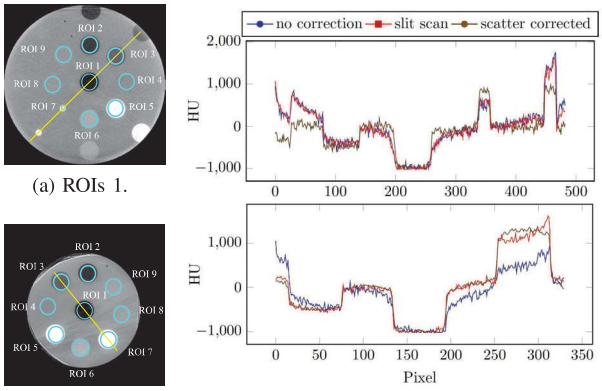

(a) ROIs 1. (b) ROIs 2. (c) Line profiles.

Fig. 8: ROIs and line profiles of the reconstructions. Top: Experiment 1 with ASG. Bottom: Experiment 2 with ASG.

regions of dense material. This is due to the photon starvation effect, which is amplified by the scatter correction when the estimated scatter signal is subtracted from these regions. Further, the combination of the C-arm iPMSE method with the ASG were investigated in Experiment 1, but its use proved to have little effect on the reconstruction results. The slit scan with our clinical scanner proved insufficient as a reference since the narrowest slit of around 20 mm in the isocenter is too wide. Also, overall evaluation is affected by the noise suppression, which is subsequent to the scatter correction. To date, such experiments have been performed with phantom data only. In future studies, we endeavor to acquire real clinical data to further examine the performance of our method, since a lack of a scatter estimate for reference purposes complicated any quantitative evaluation of said method. Further, the occurring streak artifacts have to be investigated in more detail.

V. Conclusion

The present work has proposed a novel scatter correction approach for a clinical C-arm CBCT by extending an existing method using a primary modulator. The challenges behind C-arm motion and tube current modulation were overcome with establishing a modulator database, approximating the amplitudes and a final registration step. We have shown that scatter correction using a primary modulator is possible on a C-arm system, whereby scatter artifacts were able to be removed from the reconstructions.

Acknowledgment

The authors are grateful for the financial support from the NIH Shared Instrument Grant S10 RR026714 supporting the zeego@StanfordLab, the German Research Foundation (DFG), as part of the Research Training Group 1773 “Heterogeneous Image Systems” and DAAD.

References

[1] L. Zhu, J. Wang, and L. Xing, “Noise suppression in scatter correction for cone-beam CT.” *Medical physics*, vol. 36, no. 2009, pp. 741–752, 2009.

[2] E.-P. Rührnschopf and K. Klingenbeck, “A general framework and review of scatter correction methods in x-ray cone-beam computerized tomography. Part 1: Scatter compensation approaches,” *Medical physics*, vol. 38, no. 7, pp. 4296–4311, 2011.

[3] J. H. Siewerdsen, D. J. Moseley, B. Bakhtiar, S. Richard, and D. A. Jaffray, “The influence of antiscatter grids on soft-tissue detectability in cone-beam computed tomography with flat-panel detectors.” *Medical physics*, vol. 31, no. 12, pp. 3506–3520, 2004.

[4] J. A. Sorenson and J. Floch, “Scatter rejection by air gaps: an empirical model,” *Medical Physics*, vol. 12, no. 3, pp. 308–316, 1985.

[5] J. H. Siewerdsen, M. J. Daly, B. Bakhtiar, D. J. Moseley, S. Richard, H. Keller, and D. A. Jaffray, “A simple, direct method for x-ray scatter estimation and correction in digital radiography and cone-beam CT,” *Medical Physics*, vol. 33, no. 1, pp. 187–196, 2006.

[6] M. Zellerhoff, B. Scholz, E.-P. Ruehrnschopf, and T. Brunner, “Low contrast 3D-reconstruction from C-arm data,” *SPIE Medical Imaging*, vol. 5745, pp. 646–655, 2005.

[7] L. Zhu, N. R. Benett, and R. Fahrig, “Scatter correction method for x-ray CT using primary modulation: Theory and preliminary,” *Medical Imaging IEEE*, vol. 37, no. 2, pp. 934–946, 2006.

[8] J. S Maltz, W.-E. Blanz, D. Hristov, and A. Bani-Hashemi, “Cone beam X-ray scatter removal via image frequency modulation and filtering.” *Engineering in Medicine and Biology Society, 2005. IEEE-EMBS 2005*, vol. 2, pp. 1854–1857, 2005.

[9] L. Ritschl, R. Fahrig, M. Knaup, J. Maier, and M. Kachelrieß, “Robust primary modulation-based scatter estimation for cone-beam CT.” *Medical physics*, vol. 42, no. 1, p. 469, 2015.

[10] R. Fahrig, R. Dixon, T. Payne, R. L. Morin, A. Ganguly, and N. Strobel, “Dose and image quality for a cone-beam C-arm CT system.” *Medical physics*, vol. 33, no. 12, pp. 4541–4550, 2006.

[11] A. Maier, H. G. Hofmann, M. Berger, P. Fischer, C. Schwemmer, H. Wu, K. Müller, J. Hornegger, J.-H. Choi, C. Riess, A. Keil, and R. Fahrig, “CONRAD - A software framework for cone-beam imaging in radiology,” *Medical Physics*, vol. 40, no. 11, p. 111914, 2013.

[12] C. Schmidgunst, D. Ritter, and E. Lang, “Calibration model of a dual gain flat panel detector for 2D and 3D x-ray imaging.” *Medical physics*, vol. 34, no. 9, pp. 3649–3664, 2007.

[13] H. Gao, L. Zhu, and R. Fahrig, “Modulator design for x-ray scatter correction using primary modulation: material selection.” *Medical physics*, vol. 37, no. 8, pp. 4029–37, 2010.